Correction and Characterization of Radio Frequency Interference Signatures in L-Band Synthetic Aperture Radar Data

Franz J. Meyer, *Member, IEEE*, Jeremy B. Nicoll, *Member, IEEE*, and Anthony P. Doulgeris, *Member, IEEE*

Abstract—**Radio frequency interference (RFI) is a known issue in low-frequency radar remote sensing. In synthetic aperture radar (SAR) image processing, RFI can cause severe degradation of image quality, distortion of polarimetric signatures, and an increase of the SAR phase noise level. To address this issue, a processing system was developed that is capable of reliably detecting, characterizing, and mitigating RFI signatures in SAR observations. In addition to being the basis for image correction, the robust RFI-detection algorithms developed in this paper are used to retrieve a wealth of RFI-related information that allows for mapping, characterizing, and classifying RFI signatures across large spatial scales. The extracted RFI information is expected to be valuable input for SAR-system design, sensor operations, and the development of effective RFI-mitigation strategies. The concepts of RFI detection, analysis, and mapping are outlined. Large-scale RFI mapping results are shown. In case studies, the benefit of detailed RFI information for customized RFI filtering and sensor operations is exemplified.**

Index Terms—**Calibration, error correction, L-band, radar remote sensing, radio frequency interference (RFI), synthetic aperture radar (SAR).**

I. INTRODUCTION

RADIO frequency interference (RFI) has long been identified as a problem in L-band synthetic aperture radar (SAR), limiting the performance, and applicable signal bandwidth of SAR in many areas around the globe [1]. Most RFI are incoherent electromagnetic interference signals emitted by communication systems, television networks, air-traffic surveillance radars, and other mainly military-based radiation sources whose operating frequency overlaps with the frequency band of a SAR system. RFI usually appear as various kinds of bright linear features in the azimuth-time range-frequency diagram of a SAR dataset and the interference-to-SAR signal ratio is often high.

Incoherent RFI will be partly mitigated by the matched filter process that is applied in the SAR image focusing due to

the large coherent signal-processing gain of the matched filter operation. Despite this mitigating effect, high-power RFI will remain in the focused image as visible and spatially changing signal noise. In many cases, it was shown that uncompensated RFI reduce the SAR image quality, affect the integrity of polarimetric signatures, and increase the noise level of the SAR-phase observations [2]–[4].

Several algorithms for RFI mitigation from SAR have been developed throughout the recent decades [2], [4]–[11]. The performance of these algorithms is defined by two aspects: 1) the method used for RFI detection, and 2) the approach applied for RFI removal. Finding widely applicable solutions to these two problems is difficult, as the time-frequency characteristics of RFI vary strongly across time and space.

In this paper, a processing system is presented that is successful in detecting and removing a wide range of RFI signatures that are commonly observed in L-band SAR data. In developing the processing system, emphasis was placed on improving RFI detection methodology, while RFI removal is done based on conventional incoherent notch-filtering algorithms. The superior performance of the developed RFI detection and mitigation algorithms is analyzed through a comparison with RFI mitigation methods implemented in operational SAR-processing systems. In contrast to most other RFI studies, the robust RFI detection algorithms developed in this research are additionally used to retrieve a wealth of RFI-related information that allows mapping, characterizing, and classifying RFI signatures with high spatial resolution and across large spatial scales. The developed processing system is applied to L-band SAR data of the Phased Array type L-band Synthetic Aperture Radar (PALSAR) onboard the Advanced Land Observing Satellite (ALOS). Vast parts of the ALOS PALSAR archive over North America were reprocessed for RFI correction and mapping. It is shown in this paper that the extracted RFI information provides valuable input for the design and operation of SAR systems, and for the development of effective RFI mitigation strategies.

After a short introduction of commonly observed RFI signatures in L-band SAR data (Section II), the developed custom processing system for RFI mitigation and analysis is introduced in Section III. Specific emphasis is placed on a newly developed two-stage RFI detector (Section III-B) and an RFI analysis and mapping concept (Section III-C). The performance of the developed RFI mitigation algorithms
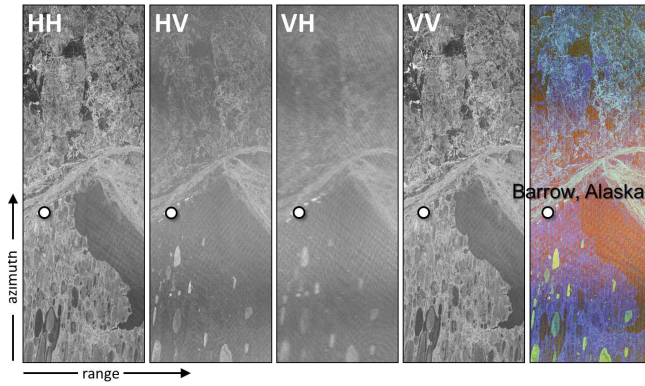
Fig. 1. RFI-affected full-polarimetric ALOS PALSAR frame acquired near Barrow, Alaska. The first four images show the four polarimetric bands of the SAR acquisition while the fifth image shows a combination of these polarimetric bands using a Pauli decomposition. RFI distortions are particularly evident in the HV and VH bands causing blurriness of these channels as well as small-scale distortions. The Pauli image shows RFI-artifacts in polarimetric information. RFI introduced strong large-scale (red band in the center of the image) and small-scale (striped and cross-hatched pattern) signature variations.

is analyzed in Section IV where the image quality, polarimetric integrity, and SAR-phase quality achieved by our custom algorithms are compared to the performance of the operational ALOS PALSAR processor. In Section V, examples of the amount and relevance of retrievable RFI information are shown and the value of this information is analyzed for selected test areas. Section VI summarizes the main findings of this paper.

II. MOTIVATION: RFI SIGNATURES IN L-BAND SAR

A. Residual RFI Signatures in Operationally Processed SAR Data

This paper on RFI in L-band SAR data was initially motivated by the presence of a large number of unsuccessfully filtered interference signals in L-band ALOS PALSAR data. RFI artifacts were particularly noticeable in the American Arctic, where the SAR image quality and polarimetric fidelity appeared significantly impaired across wide areas. Fig. 1 shows a typical example of RFI-induced distortions in a SAR image acquired over Barrow, Alaska. Shown are the four bands of fully polarimetric ALOS PALSAR frame ALP-SRP172601440 together with a Pauli decomposition image that was produced from these data. The location of Barrow, Alaska, is identified in the images. Image frame ALP-SRP172601440 is used throughout this paper to demonstrate RFI contamination and exemplify RFI mitigation performance.

RFI-related image distortions are particularly evident in the HV and VH channels of the PALSAR frame in Fig. 1. This is due to the lower signal power in the cross-polarized images and the corresponding higher RFI-to-signal ratio in these channels. Especially in HV and VH, the following typical RFI artifacts can be seen [5], [12].

1) As incoherent RFI are smeared during image focusing, RFI often cause haze-like image artifacts that appear superimposed onto the focused SAR image. The intensity of these hazy signatures can vary with azimuth time

if the time-frequency pattern of the RFI is not stationary. Such slowly varying hazy artifacts are evident in the HV and VH channels of Fig. 1.

2) Additional small-scale image patterns can appear whenever the RFI patterns in the SAR raw data were irregular. After convolution with the matched filter kernel, small-scale image artifacts like the linear and cross-hatched patterns in the images of Fig. 1 can be created. Artifacts are stronger in the cross-pol channels, but are still visible in darker patches of the co-pol images.

3) Under certain circumstances, the presence of RFI can also interfere with the image-focusing process. For example, if some parameters of the matched filter (e.g., the azimuth frequency modulation rate) are estimated from the data itself, the presence of high-powered incoherent RFI can cause this estimation to yield biased results. If focused with biased and matched filter parameters, the image remains blurry (see bottom part of the VH channel in Fig. 1 for an example).

Please note that the RFI distortions in the individual polarimetric channels shown in Fig. 1 are not identical. The RFI signature is linked to the polarization of the receive channel and is usually different in vertical- and horizontal-receive polarizations, depending on the transmission characteristics of the RFI emitter. Therefore, the RFI signatures are usually different in HV and VH, but identical in HH and VH. A close examination of the dark image patch in the lower right segment of the image frame in Fig. 1 confirms this statement. In this area, the RFI-induced small-scale artifacts have a cross-hatched pattern in HH and VH but follow a linear pattern in VV and HV.

As the RFI distortions in the four channels of a full-polarimetric image are different, the presence of RFI also causes distortions of the polarimetric information captured in the SAR data. The Pauli decomposition image of frame ALP-SRP172601440 on the right-hand side of Fig. 1 shows such distortions. While some of the color information in the Pauli decomposition image is due to the scattering properties of real surface features (e.g., lakes in the bottom half of the image), the RFIs have introduced strong large-scale (red band in the center of the image) and small-scale (linear and cross-hatched patterns) signature variations into the polarimetric data. As will be shown later (see Section IV-C and Fig. 10), RFI-related distortions can have detrimental effects on polarimetric classification methods that are often applied to polarimetric SAR data.

The difficulty in automatic detection and mitigation of RFI signatures in SAR data arises from the wide range of time-frequency patterns that RFI can exhibit. Fig. 2 shows two examples of commonly observed L-band RFI signatures showcasing this diversity in time-frequency characteristics. Fig. 2(a) shows 6000 lines of the ALOS PALSAR image in Fig. 1 in a range-frequency azimuth-time representation. The HV channel is shown and the regular SAR image information can be identified by the relatively homogeneous background power. The bright stripes in Fig. 2(a) correspond to RFIs that are superimposed on the SAR image information. In this example, the RFIs have relatively wide bandwidths of several
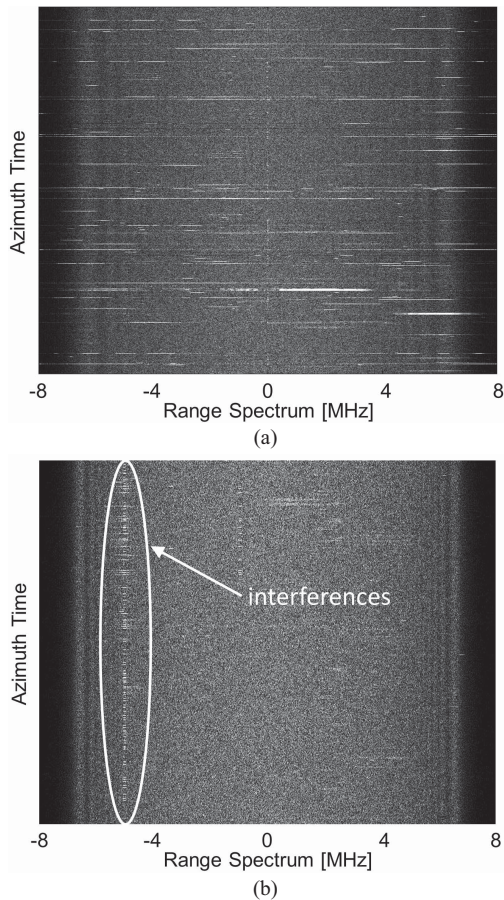
Fig. 2. Examples of L-band RFI signatures with different time-frequency characteristics. (a) Data acquired over Barrow, Alaska, containing time varying wide-band (TVWB) RFI. The RFIs appear as bright stripes superimposed onto the image signal. (b) Interference in the Canadian Arctic of time stationary narrow band (TSNB) nature. The location of the RFI is highlighted.

MHz and exhibit an almost random variation of center frequencies along azimuth time. These time-varying wide-band (TVWB) RFI are often found in areas along the American Arctic coast. In contrast, the data in Fig. 2(b), acquired over the Canadian Northwest Territories, show RFI of different, almost orthogonal properties. Here, the interferences are time-stationary narrow-band (TSNB) features. These two examples can be understood as end members of a larger family of RFI signatures whose properties are a combination of the examples shown in Fig. 2. Operational RFI filters need to address the large diversity of RFI time-frequency behaviors to be able to filter all RFI types with similar quality, and guarantee consistent data quality across large spatial scales.

B. Goals of This Research

The presence of wide-spread RFI distortions in global operationally processed L-band SAR archives and the growing diversity of interfering RFI signatures give rise to the two main goals of this research.

1) Development of improved RFI detection and correction technology to support reliable RFI correction and contribute to high-quality and consistent SAR data archives. A robust RFI detection scheme also allows reliable

documentation of the time-frequency behavior of RFI signals in an image frame.

2) Global RFI characterization, mapping, and monitoring to evaluate the spatial distribution of RFI strength and RFI characteristics and to analyze changes of RFI load over time. In particular, a global characterization and tracking of time-frequency properties of RFI can be the basis for location-based RFI-filter algorithms that are optimized for the RFI properties in a specific geographic location. An analysis of the temporal evolution of RFI can provide important information for a policy making in defense of the microwave bands allocated for remote sensing.

These overarching goals were the main drivers in the definition of the RFI processing system that is introduced and evaluated in the following sections.

III. CUSTOM PROCESSOR FOR RFI MITIGATION AND CHARACTERIZATION

A customized SAR-processing system was developed that is optimized for reliable detection and removal of a wide range of RFI signatures that are commonly observed in L-band SAR data. Particular emphasis was put on: 1) the development of a robust RFI detection algorithm, and 2) the implementation of an RFI analysis concept that extracts, archives, and maps interference properties to create a geographically referenced RFI data base.

A. RFI Signal Considerations and SAR Processor Workflow

In the presence of RFI, and if the useful signal, system noise, and interfering signals are denoted as s, n, and r, respectively, then the (unfocused) SAR measurement at the fast time τ and slow time t can be written as

$$h(t, \tau) = s(t, \tau) + n(t, \tau) + r(t, \tau). \tag{1}$$

The goal of RFI detection and suppression is then to find efficient ways to automatically detect and remove r given h.

As RFI signals are usually narrow-band compared to the bandwidth of the SAR signal s, the interference-to-signal plus noise ratio (ISR) is optimized by transforming the data into the range-frequency azimuth-time domain $H^\nu(t, \nu)$ using a 1D Fourier transform that converts fast time τ into range frequency ν. In this domain, the usually high ISR supports RFI detection. Therefore, RFI detection and suppression is performed in $H^\nu(t, \nu)$ in our approach.

The RFI detection, characterization, and mitigation concept presented in this paper are embedded into a SAR processor that follows a Range-Doppler processing concept [13]. The workflow of the developed processing system is presented in Fig. 3. After range compression and differential range cell migration correction (RCMC), the SAR data are transformed into the range-frequency azimuth-time domain. There, a two-step RFI detection and mitigation filter is applied. As seen in Fig. 3, the detected interference signatures are logged in image-specific log files, which are further processed in a postprocessing RFI analysis step and converted to geographically referenced RFI information.
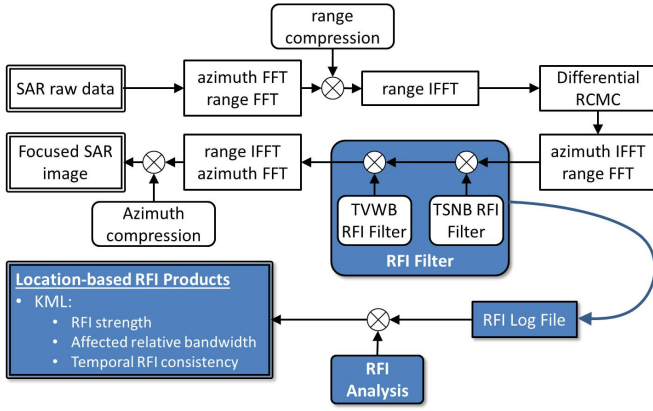
Fig. 3. Workflow of the custom processor for RFI mitigation and analysis.

Performing RFI detection after RCMC has two main advantages: 1) as RFI transmitters can often be considered point sources, their transmitted signal follows the usual range curvature in the unfocused data. After RCMC, RFI signatures form straight lines in $H^v(t, v)$, increasing the performance of the RFI filters introduced in Section III-B, and 2) performing the RFI analysis late in the processing flow is advantageous as it makes it easy to perform RFI correction from a fully focused complex SAR image. Often, SAR users will only have access to fully focused single look complex (SLC) data rather than the raw SAR acquisitions. Using the proposed processing concept, only the last step of SAR image focusing (azimuth compression) needs to be reversed to be able to perform high performance RFI suppression [5].

B. RFI Detection Concept

Acknowledging the diverse time-frequency characteristics of RFI, a detection concept was developed that operates on $H^v(t, v)$ and relies on a combination of two RFI detectors with near-orthogonal properties. A first filter is optimized for TSNB interference signatures and is effective in detecting RFI signatures like the example in Fig. 2(b). The second filter, applied consecutively, is optimized for time-varying wide-band (TVWB) signals, and has orthogonal sensitivity properties. As the TSNB and TVWB RFI types can be understood as end members of a larger family of RFI signatures whose properties are a combination of these end member types, the combination of TSNB and TVWB filters is expected to be effective in detecting a wide range of interference structures.

C. TSNB RFI Detector

To detect TSNB RFI, the average range power spectrum $|H^v(v)|^2$ of the observed signal $H^v(t, v)$ is estimated by averaging blocks of 256 azimuth lines. In the absence of RFI, and if no weighting was applied on the transmitted range chirp, the average range spectrum $|H^v(v)|^2$ is flat within the signal bandwidth B_r [Fig. 4(a)], and has Gaussian properties. This Gaussian nature is exemplified in Fig. 4(b), where the probability density function (PDF) of the data in Fig. 4(a) is shown in a log-likelihood plot.

Due to their temporal consistency, TSNB RFIs form peaks in the averaged range spectrum and can be detected if their
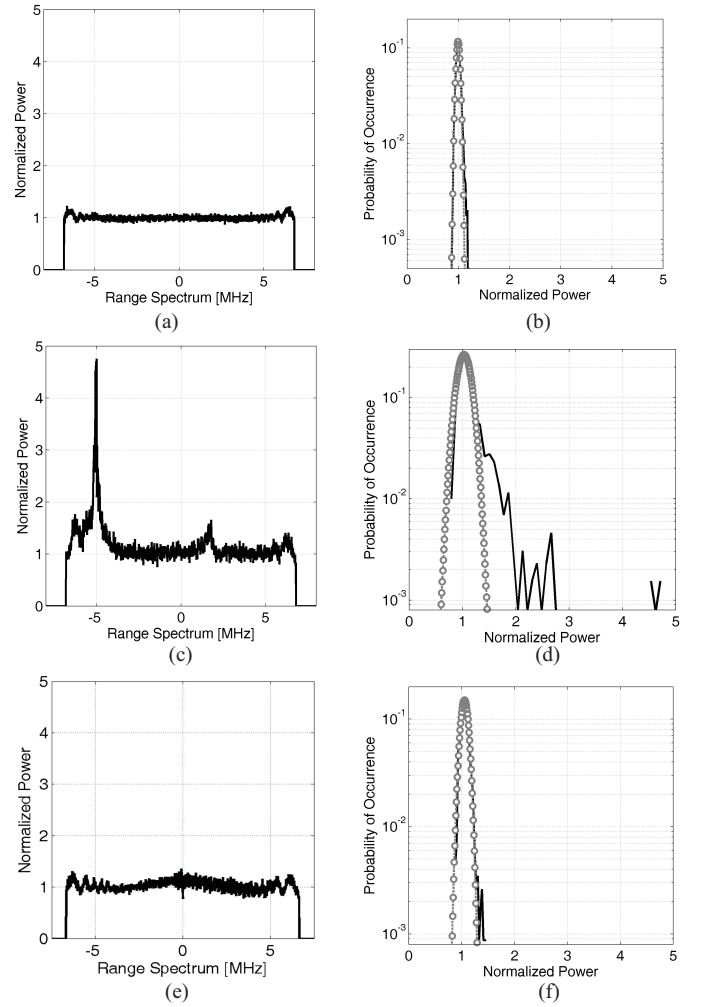

Fig. 4. Range Power spectra estimated from 256 azimuth lines. (a) Power spectrum of an RFI-free PALSAR data set. (c) Power spectrum of the RFI-affected SAR data shown in Fig. 2(b). (e) Power spectrum of the SAR data in Fig. 2(a). (b), (d), and (f) show PDFs of the data in (a), (c), and (e), respectively. The PDFs (black lines) are shown in a log-likelihood presentation and are augmented with the best fitting Gaussian approximation (gray). It can be seen that the PDFs in (b) and (f) are of Gaussian nature. While the PDF in (d) is affected by outliers, its main lobe is still near Gaussian.

average power significantly deviates from the Gaussian distributed background clutter. An example of TSNB RFI-affected data can be found in Fig. 4(c) where the average range spectrum $|H^v(v)|^2$ of the data in Fig. 2(b) is shown. The time-consistent RFIs in this dataset form easily identifiable peaks in $|H^v(v)|^2$ and cause a long tail in the PDF of $|H^v(v)|^2$ [shown in Fig. 4(d)]. As the main lobe of the PDF still follows a Gaussian distribution, a one-tailed Fisher's Z-test [14] can be applied to detect RFI by calculating

$$Z = \frac{|H^v(v)|^2 - \mu_{H(v)}}{\sigma_{H(v)} \sqrt{1/256}} \tag{2}$$

and comparing Z to a critical value that is selected for a confidence level of $1 - \alpha = 99.5\%$. Fisher's Z-test belongs to the group of parametric statistical hypothesis tests where the null hypothesis $H_0 : |H^v(v)|^2 = \mu_{H(v)}$ is tested for validity given a predefined statistical significance level α. Here, α describes the likelihood of the null hypothesis H_0 being rejected when true, corresponding to the likelihood

of incorrectly classifying image signal as RFI. A small α level minimizes such so-called type I errors but increases the likelihood of committing related type II errors, which describe the chance of real RFI being missed in the detection. In our cases, α was optimized in empirical tests to minimize the sum of type I and type II errors. The symbols $\mu_{H(\nu)}$ and $\sigma_{H(\nu)}$ in (2) denote the mean and standard deviation of the best fitting Gaussian approximation to the data in $|H^\nu(\nu)|^2$ (shown in Fig. 4(d) as gray dashed line). After $\mu_{H(\nu)}$ and $\sigma_{H(\nu)}$ were estimated from the data, (2) is evaluated and the derived Z value is used to detect the RFI.

The estimates of $\mu_{H(\nu)}$ and $\sigma_{H(\nu)}$ may be biased if the percentage of RFI-affected samples in the analyzed data is high. To minimize potential biases, a robust estimation method was implemented: Instead of calculating $\mu_{H(\nu)}$ and $\sigma_{H(\nu)}$ from the full sample, a trimmed mean and standard deviation is calculated [15], where the first $r/2$ largest and first $r/2$ smallest observations are trimmed before calculating $\mu_{H(\nu)}$ and $\sigma_{H(\nu)}$. In our approach, r is set to 1% of the sample size, leading to truncation points near the $\mu_{H(\nu)} - 2.5\sigma_{H(\nu)}$ and the $\mu_{H(\nu)} + 2.5\sigma_{H(\nu)}$ location. This setup rejects most outliers in the calculation of $\mu_{H(\nu)}$ and $\sigma_{H(\nu)}$ while keeping distortions to the image data distribution minimal [16], [17].

Variants of the TSNB RFI detector have been used before. For instance, a variant of the TSNB detector is included in the operational ALOS PALSAR processor [1]. The advantage of our implementation lies in the definition of the detection thresholds, where, instead of using a fixed threshold, detection thresholds are selected automatically and dynamically based on the statistical properties of the data. A short description of the ALOS PALSAR RFI detector is provided in Section IV-A.

D. TVWB RFI Detector

A second filter is necessary as TVWB signatures like the ones shown in Fig. 2(a) tend to disappear in the averaged range power spectra $|H^\nu(\nu)|^2$. For example, Fig. 4(e) shows the 256 line-averaged range power spectrum of the data in Figs. 2(a) and 1. Due to their randomly changing center frequency, the RFIs in Fig. 2(a) cancel out in the averaging process included in the calculation of $|H^\nu(\nu)|^2$. Fig. 4(f) indicates that the TVWB RFI does not deviate from the background PDF and cannot be detected by the previously introduced TSNB detector.

Due to their wide bandwidth nature, TVWB can best be identified by averaging $H^\nu(t, \nu)$ in a range-frequency direction rather than along the azimuth time. Blocks of 100 range-frequency samples are averaged to yield the average signal power along azimuth time $|H^\nu(t)|^2$ (see Fig. 5(a) for a segment of $|H^\nu(t)|^2$ calculated from the data shown in Fig. 1). To approximate stationarity, $|H^\nu(t)|^2$ is detrended by subtracting a best-fitting slope $\hat{a}$ from the data

$$|H^\nu(t)|_d^2 = |H^\nu(t)|^2 - \hat{a} \cdot t. \tag{3}$$

Due to the central limits theorem, $|H^\nu(t)|_d^2$ is a Gaussian signal, and a Fisher's Z-test, according to

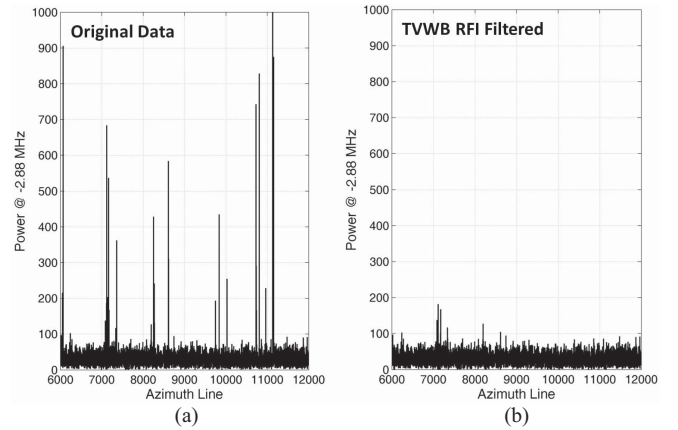$$Z = \left(|H^\nu(t)|_d^2 - \mu_{H(t)} \right) \Big/ \sigma_{H(t)} \sqrt{1/100} \tag{4}$$

Fig. 5. (a) Visualization of the variation of signal power in a slice through $H^\nu(t, \nu)$ along azimuth. One hundred range-frequency samples are averaged and detrending for amplitude variations was performed, yielding $|H^\nu(t)|_d^2$. Narrow peaks in the plot are due to RFI; after (b) TVWB notch filtering most of the interfering signals were removed.

can be applied for TVWB RFI detection. RFI detection is done based on a confidence level of $1 - \alpha = 99.5\%$ and the previously introduced robust estimation techniques are used for the calculation of $\mu_{H(t)}$ and $\sigma_{H(t)}$.

Fig. 5(b) shows the data in Fig. 5(a) after TVWB RFI filtering to demonstrate the effectiveness of the proposed procedure. It can be seen that most of the RFIs in this dataset were found and removed.

E. Denoising of Initial Detections

As initial RFI detection is done using statistical hypothesis-testing procedures, there is a likelihood of $\alpha = 0.5\%$ for the image data samples to be incorrectly classified as RFI. These false detections cause noise in the raw binary detection matrix that needs to be removed in order to avoid the filtering of too much signal from the observed SAR raw-data matrix. In addition to false RFI detections, RFI frequency elements may be missed in the detection process if the ISR varies throughout the dataset. After RCMC, the RFI form linear structures in $H^\nu(t, \nu)$. Hence, the removal of false RFI detections and the completion of missing RFI elements can be performed using a Radon transform or the computationally more efficient Hough transform [18]. The Hough transform is optimized for finding parameters of line elements that are present in noisy binary images. The main advantage of the Hough transform is that it is tolerant of gaps in the original detection masks and is relatively unaffected by image noise. A good introduction to the Hough transform can be found in [19]. Using the Hough transform, linear RFI structures in the initial detection mask are detected and retained, while noise elements are rejected. A result of the Hough-based denoising operation is shown in Fig. 6 where original RFI detections for 12 000 lines of a PALSAR image are shown in Fig. 6(a). The Hough-based denoising results in Fig. 6(b) show a clear reduction of noise while full retention of RFI signals was achieved. Also, gaps in original detections were closed by the Hough operation.
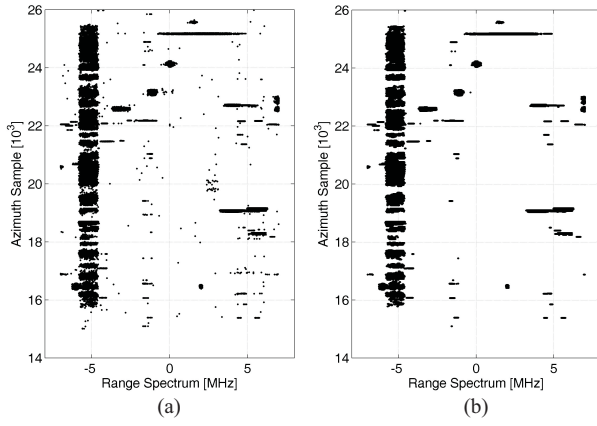
Fig. 6. (a) Raw RFI detection before Hough-based denoising was applied. Twelve thousand lines of a PALSAR data set are shown; after (b) Hough-based denoising, noise is successfully suppressed while correct RFI signatures are retained and completed.

TABLE I

EXAMPLE OF AN RFI METADATA FILE THAT IS PRODUCED BY THE RFI CHARACTERIZATION AND MAPPING PROCESSOR. CHARACTERISTICS OF RFI CONTAINED IN PALSAR GRANULE ALPSRP172601440 ARE SHOWN

RFI Type [1 = TVWB; 2 = TSNB]:	1.00
RFI Range Bandwidth - MODE [MHz]:	0.5
RFI Range Bandwidth - MEAN [MHz]:	1.1
RFI Range Bandwidth - MEDIAN [MHz]:	0.7
RFI Range Bandwidth - MAX [MHz]:	9.8
RFI Range Bandwidth - MIN [MHz]:	0.03
RFI ISR - MEAN [dB]:	48.8
Affected Lines [%]:	11.0
Affected Bandwidth ($> 0.1\%$) [%]:	100.0
Affected Bandwidth ($> 0.3\%$) [%]:	84.5
Affected Bandwidth ($> 0.5\%$) [%]:	78.4
Max. RFI-free Bandwidth ($< 0.1\%$) [MHz]:	0.0
Max. RFI-free Bandwidth ($< 0.3\%$) [MHz]:	2.0
Max. RFI-free Bandwidth ($< 0.5\%$) [MHz]:	3.1

F. RFI Mitigation

After denoising, RFI signatures detected by both detectors are removed using a conventional adaptive notch filtering approach [7], [20], [21], where the width of the notch filter is adapted to the parameters of the detected RFI. If an RFI with center frequency ν_1 and bandwidth b_1 was detected at azimuth time t_1, the notch-filtered SAR data is created by multiplication of $H^\nu(t_1, \nu)$ with a notch at ν_1

$$H^\nu_{\text{notched}}(t_1, \nu) = H^\nu(t_1, \nu) \cdot \left(1 - \frac{1}{b_1}rect\left(\frac{\nu - \nu_1}{b_1}\right)\right). \quad (5)$$

In our implementation, where a 2-D mask of notches is available after the denoising step in Section III-E, all detected RFIs are removed in one step by multiplying $H^\nu(t, \nu)$ with this 2-D notch mask.

Notch filtering is an easy to implement, widely used, and very effective method for RFI suppression in SAR data [22]. Despite its effectiveness, notch filtering can have adverse effects on the imaging performance that depends on the width of the applied notch. For instance, it can be shown that notch filtering can lead to an increase of sidelobe levels in focused SAR images and may decrease the data's signal-to-noise ratio [22]. Still, notch filtering has been the method of choice for effective and efficient RFI suppression of many operational SAR systems such as ALOS PALSAR [1].

Despite the simplicity of the RFI mitigation approach that is applied in the presented processor, it will be shown in Section IV that our custom processing system outperforms operationally used algorithms. This is mostly due to the robust RFI detection algorithms that were implemented in our system and lead to a more reliable identification of RFI signals.

G. RFI Analysis and Mapping Approach

After denoising, the final RFI detections are logged and archived for every image frame by recording their azimuth-time and range-frequency location as well as their signal power and ISR. In these log files, the interference information is augmented with information about the scene location, acquisition time and date, orbit direction, and full granule ID to enable geocoding of RFI parameters and a geospatial analysis of RFI time-frequency characteristics. A variety of RFI parameters are calculated from the log files and are both stored in metadata files and converted into color-coded keyhole markup language (KML) files for geo-referenced visualization in Google Earth. The RFI parameters derived for every analyzed SAR image acquisition include the following.

1) Percentage of RFI-Affected Lines $\text{RFI}_t^\%$: The image lines containing RFI detections at any frequency are counted and divided by the total number of lines per image. $\text{RFI}_t^\%$ provides information on the RFI load in an image.

2) Percentage of Affected Bandwidth $\text{RFI}_{B_\nu}^\%$: The RFI range-frequency PDF is calculated, expressing the likelihood of an image line to contain an RFI at range frequency ν. Frequencies with likelihoods above a predefined threshold are considered RFI-affected and the percentage of affected bandwidth can be calculated.

3) Average RFI bandwidth $\mu(B_{\text{RFI}})$: RFI bandwidths are calculated from the range-frequency extent of extracted RFI patterns and the arithmetic mean of RFI bandwidths is calculated per image frame. From a combination of $\text{RFI}_{B_\nu}^\%$ and $\mu(B_{\text{RFI}})$, conclusions on the RFI type (TSNB or TVWB) can be drawn.

4) Maximum RFI bandwidth $\max(B_{\text{RFI}})$: As the probability density function of the RFI range bandwidth is usually heavily right-skewed, parameter $\mu(B_{\text{RFI}})$ is only an incomplete description of the RFI-bandwidth behavior. Hence, the maximum RFI-bandwidth $\max(B_{\text{RFI}})$ is calculated to augment $\mu(B_{\text{RFI}})$. $\max(B_{\text{RFI}})$ corresponds to the largest RFI bandwidth detected in an image frame.

5) Maximum-free Bandwidth [MHz] $\max(B_{\text{free}})$: In the RFI range-frequency PDF, unaffected bandwidth segments are defined as the frequency elements for which the PDF dips below a predefined threshold. Out of all the identified segments, the longest segment is extracted and recorded to indicate the maximum RFI-free frequency band.

Table I shows an example of the statistical RFI information that is currently extracted for each analyzed granule.
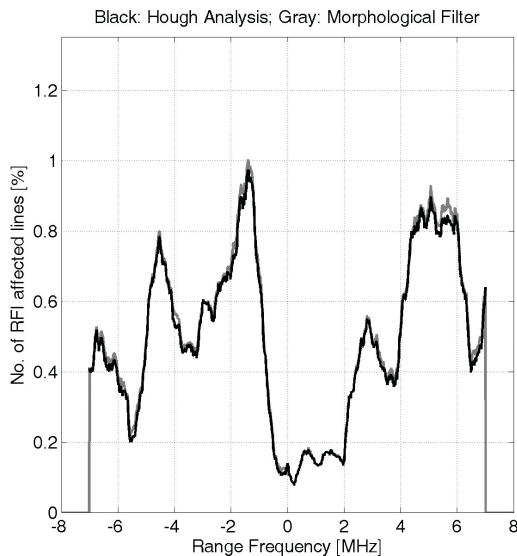
Fig. 7. Range-frequency distribution of RFI detected in PALSAR granule ALPSRP172601440. Per frequency component, the percentage of lines that carry interference at this frequency is shown.

The characteristics of RFI in PALSAR granule ALP-SRP172601440 are shown. Analysis results include an assessment of RFI type (TVWB or TSNB), several measures of central tendency of the RFI bandwidth PDF, maximal and minimal RFI bandwidth, mean ISR, percentage of affected lines $\text{RFI}_t^\%$, percentage of affected bandwidth $\text{RFI}_{B_v}^\%$ calculated for three different thresholds (0.1%, 0.3%, 0.5%), and the maximal RFI-free bandwidth $\max(B_{\text{free}})$ calculated for the same thresholds. As the full RFI information is available for every image from the logging algorithms in the processor, more RFI parameters can be added to the pool of retrieved RFI information at any time if the current set of parameters is deemed incomplete or if new RFI patterns are identified.

In addition to the numerical information, a series of plots are created including plots of the RFI-range bandwidth PDF, RFI range-frequency distribution, and the PDF of the ISR. A plot of the RFI range-frequency distribution is shown in Fig. 7 for granule ALPSRP172601440. This plot shows the likelihood of encountering interference at a given range-frequency element of an image line. Plots like this can be used in conjunction with the information in Table I to analyze RFI behavior and develop adaptive methods for RFI correction.

The information shown in Table I is also geocoded and converted into large-scale maps to enable the spatial analysis of RFI properties as well as the correlation of detected RFI patterns with transmitter locations and population centers. A large-scale RFI-mapping result produced by the developed processing system is shown in Fig. 8. There, the spatial distribution of the $\text{RFI}_t^\%$ parameter is displayed for extended areas of the Arctic as well as the entire U.S. mainland. The $\text{RFI}_t^\%$ information is color coded with green corresponding to $\text{RFI}_t^\% = 0\%$ and red corresponding to $\text{RFI}_t^\% > 10\%$. Strong RFI presence can be identified across the American Arctic, in Florida, across extended areas of Texas and New Mexico, and in the American Mid-West. Additionally, more localized RFI-affected regions include the U.S. west coast
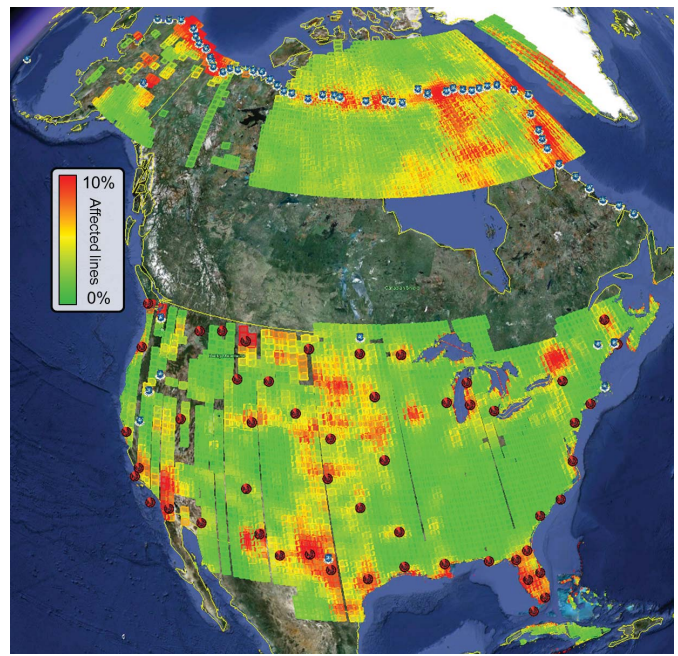

Fig. 8. Spatial distribution and strength of RFI in ALOS PALSAR images over North America. The bounding boxes show the geographic location of analyzed ALOS PALSAR data frames. The red and blue markers show locations of known radar transmitters.

and the area around Ottawa. In addition to the RFI information, the locations of the known ground-based L-band radar transmitters for two ground-based transmitter networks are shown. Blue symbols show locations of long-range and short-range over-the-horizon radars of the North Warning System. Red circular symbols identify radar stations operated by the Federal Aviation Administration (FAA). From Fig. 8, it can be seen that areas of increased RFI are generally coincident with known locations of these radars. It can also be seen that some areas are affected by RFI from currently unknown sources; their locations do not coincide with the location of the above identified RFI emitters. Also, a few known L-band emitters did not cause identifiable RFI in the analyzed PALSAR data. There are many potential reasons for either case, including inactivity of the RF emitter during the PALSAR observation times or transmission at L-band frequencies outside of the bandwidth used by PALSAR.

A detailed analysis of the RFI characteristics at selected RFI-prone test sites is presented in Section V. There, the benefit of the logged RFI information for automatic classification and characterization of RFI sources as well as for this paper of temporal RFI consistency is shown.

IV. VALIDATION OF RFI MITIGATION PERFORMANCE

To demonstrate the effectiveness of the developed RFI detection and mitigation algorithms, RFI-affected full-polarimetric ALOS PALSAR data were processed using both the operational PALSAR-processing stream and the customized processor presented in Section III. Processing results were then analyzed for a relative image quality, polarimetric integrity, and phase noise levels to assess the relative performance of the implemented RFI mitigation methods.
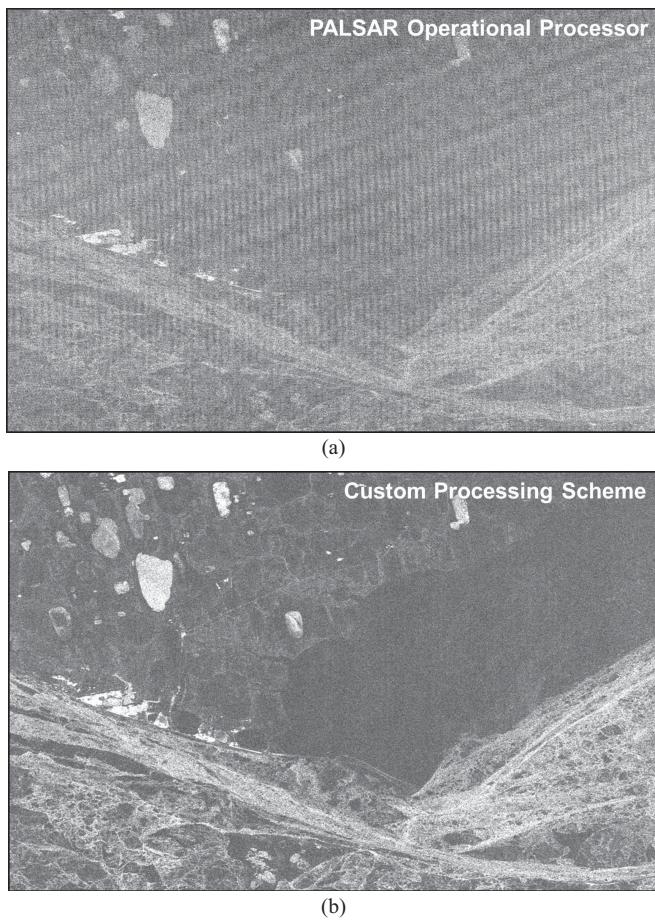
Fig. 9. (a) HV channel of an operationally processed, and (b) custom-processed image acquired near Barrow, Alaska. The operational processor does not remove all image artifacts while the proposed algorithms dramatically improve image quality.
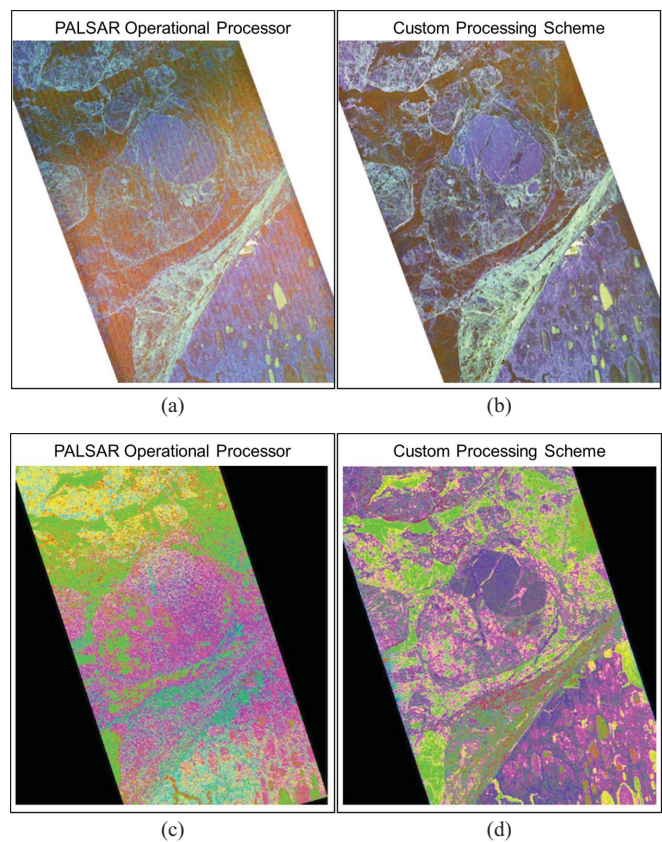

Fig. 10. Improvement of polarimetric signature exemplified by a polarimetric clustering example. (a) and (b) show before-and-after Pauli RGB images. (c) and (d) show before-and-after the segmented class images. The proposed filtering algorithm results in flatter response, sharper detail, and better defined clusters.

A short summary of the reference RFI mitigation concept is provided in Section IV-A, followed by a presentation of achieved performance improvements.

A. Short Summary of the ALOS PALSAR RFI Detection and Mitigation Concept

The operational PALSAR processor uses an RFI detection scheme that is similar to the TSNB RFI detector that was introduced in Section III-C. The average range power spectrum of the observed signal $H^\nu(t, \nu)$ is estimated by averaging the blocks of 256 azimuth lines. To detect RFI, first the mean signal amplitude $\mu_{H(\nu)}$ is calculated using a robust estimation method similar to the trimmed mean approach [15], [17]. After $\mu_{H(\nu)}$ is calculated, a threshold is applied that classifies signal components as RFI if their signal power differs from $\mu_{H(\nu)}$ by more than 2 dB [1]. More details on the PALSAR RFI detection and mitigation concept can be found in [1] and [23].

Compared to the operational ALOS PALSAR RFI-filtering concept, we believe that the approach presented in this paper has two main advantages that optimize RFI mitigation performance: 1) in contrast to the single-filter approach of the PALSAR processor, this new RFI mitigation concept is based on two orthogonal filters and is therefore expected to improve the detection success rate compared to the operational

PALSAR processing system, and 2) the detection thresholds in this new system are determined automatically and, in contrast to the fixed threshold used in the PALSAR processor, change adaptively with the statistical properties of the data.

B. Improvements to Image Quality

The improvements in SAR image quality achieved by the customized processor are exemplified in Fig. 9. There, a 6000-line segment of the HV channel of PALSAR acquisition ALP-SRP172601440 over Barrow, Alaska, is shown. Both, operationally [Fig. 9(a)] and custom-processed [Fig. 9(b)] images are presented. Fig. 9(a) indicates significant distortions from residual RFI in the operationally processed PALSAR frame. Remaining image artifacts in the operationally processed data include visible image blurring, small-scale image artifacts, as well as a hazy brightness variation across the presented image segment. The custom processor, however, successfully removed the bulk of the RFI energy and produced a high-quality SAR image [Fig. 9(b)].

C. Correction of Polarimetric Signature

To analyze the improvements of polarimetric fidelity, a full-polarimetric PALSAR scene acquired over Barrow, Alaska was processed to a Pauli RGB image. PALSAR frame ALP-SRP168371440 was chosen here instead of the previously

used frame ALPSRP172601440 for reasons of data interpretability. While being optimal for exemplifying the image distortions and for showcasing the achieved image quality improvements, the sea ice structure in the previously used frame is very complex, making a visual interpretation of the polarimetric signal difficult. Frame ALPSRP172601440, used in Fig. 10, shows sea ice structures that are more spatially consistent. Hence, polarimetric distortions are easier to see and improvements of polarimetric fidelity are easier appreciated. The area covered by this frame includes Alaska's Arctic coast in the south-eastern corner of the image, and the ice-covered ocean throughout the rest of the image frame. Pauli images derived from operationally processed PALSAR data are shown in Fig. 10(a) while custom-processed data are presented in Fig. 10(b). The color distortions visible in Fig. 10(a) are corrected in Fig. 10(b) to virtually flat Pauli RGB images whose polarimetric signatures are now solely due to variation of surface properties.

Fig. 10(c) and (d) show the results of a clustering approach where the data of Fig. 10(a) and (b) was used to classify the imaged area into various surface classes. The clustering approach published in [24] was applied. The objective of this classification test was to analyze if the custom-processed data show improved performance in identifying different sea ice types. It is evident that the custom processor [Fig. 10(d)] produces more distinct, less blurry, and more realistic classification results that are of higher geophysical relevance.

D. Reduction of Phase Noise Levels

To determine the benefit of the custom processing algorithms for phase noise reduction, a pair of RFI-affected PALSAR images (including ALPSRP172601440 as one of the InSAR partner images) acquired near Barrow, Alaska, were processed to a SAR interferogram. As RF interference adds incoherent phase noise to the observed SAR data, insufficiently corrected RFI will increase the noise level of the interferometric phase and lead to a reduction of the interferometric coherence. Therefore, an analysis of coherence can be used to assess the relative performance of RFI mitigation methods.

For this experiment, SAR image processing was done using both the operational PALSAR processor and the custom processor shown in Fig. 3, resulting in an operationally processed and a custom-processed image pair. Both image pairs were then sent through an identical interferometric SAR (InSAR)-processing stream to generate interferograms and coherence images. After InSAR processing, coherence probability density functions were calculated for both the operationally processed and custom-processed data and a relative performance assessment was performed. Multilooking of 8×25 resolution cells (200 looks) was applied during InSAR processing to generate coherence PDF of near-Gaussian shape and ease the analysis of coherence differences. The resulting coherence PDFs are visualized in Fig. 11. It can be seen that the application of advanced RFI mitigation methods leads to a clear improvement of interferometric coherence. This indicates that the RFI detection and mitigation algorithms that are implemented in the custom processor are superior to the methods used in the operational PALSAR system.
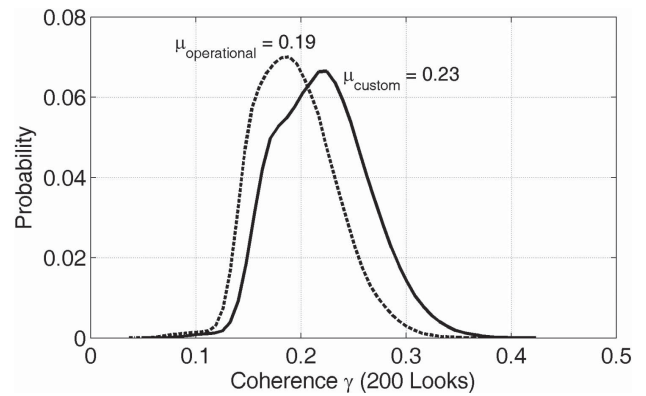

Fig. 11. Coherence PDFs for an InSAR pair of RFI-affected PALSAR images processed by both the operational (black-dashed line) and the custom (black-solid line) processors. Through customized RFI processing, a coherence improvement could be achieved.

V. RFI CHARACTERIZATION, CLASSIFICATION AND MAPPING

As mentioned previously, during the RFI filtering step of the customized SAR-processing scheme, an extensive amount of RFI information is recorded and stored in log files. Per image granule, this information is analyzed by the RFI analysis and mapping algorithms presented in Section III-C and converted to numerical information (RFI metadata) and kml-based maps that visualize spatial variation of RFI properties. In the following, a set of examples are presented that demonstrate the wealth of RFI information that is produced and indicate the benefit of this information for RFI characterization and the development of adaptive RFI correction methods.

A. RFI Characterization and Source Identification

The RFI metadata can be used in conjunction with the mapping information produced by the custom processor to: 1) characterize RFI properties for any given area; 2) to compare the properties across regions; and 3) to classify RFI signatures into classes of similar properties. Fig. 8 shows that such characterization studies can be performed on continental or even global scale if the analysis is based on a global observation system such as ALOS PALSAR.

Figs. 12 and 13 show a comparative analysis of RFI properties at two geographically separate RFI hot spots, one area located in the American Arctic near Barrow, Alaska (Fig. 12), and a second area located near Odessa, Texas (Fig. 13). Figs. 12(a) and 13(a) show the percentage of RFI-affected lines in PALSAR images over these areas (green: 0%; red: > 10%), while Figs. 12(b) and 13(b) show the maximum RFI-free bandwidth for these regions (green: > 10 MHz; red: < 1 MHz). From a comparison of Figs. 12 and 13, it can be seen that the interferences in these areas are fundamentally different, pointing to two distinctly different RFI sources.

For the RFI near Barrow, Alaska (Fig. 12), both the percentage of affected lines and the percentage of affected bandwidth are very high. The large number of affected lines points to an RFI source that transmits interference signals at a pulse repetition frequency (PRF) close to 10% of the sampling frequency of the PALSAR instrument. The large percentage of affected
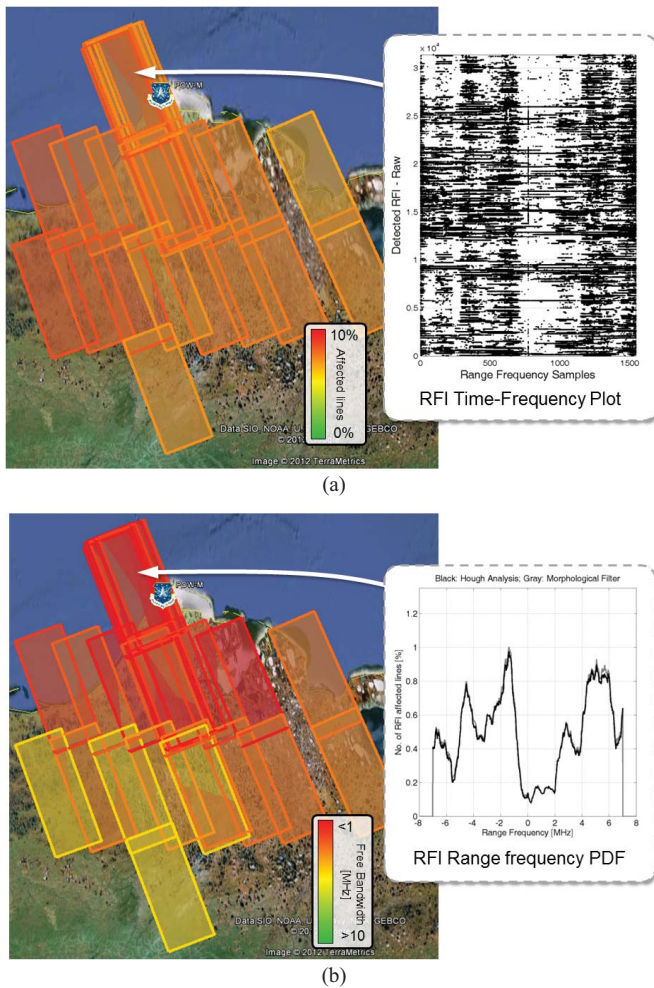
(a)

(b)

Fig. 12. RFI properties for an area near Barrow, Alaska. (a) Percentage of affected lines $\mathrm{RFI}^{\%}_{B_v}$ (green: 0%; red: >10%). A time-frequency plot of detected RFI is added for one selected image frame. (b) Maximum RFI-free bandwidth max(B_{free}) (green: >10 MHz; red: <1 MHz). Additionally, the RFI range frequency distribution is shown for a selected frame. RFI in this area is of wide bandwidth nature and affects a large percentage of lines.

(a)

(b)

Fig. 13. RFI properties for an area near Odessa, Texas. (a) Percentage of affected lines $\mathrm{RFI}^{\%}_{B_v}$ (green: 0%; red: >10%). A time-frequency plot of detected RFI is added for a selected image frame. (b) Maximum RFI-free bandwidth max(B_{free}) (green: >10 MHz; red: <1 MHz). Additionally, the RFI range-frequency distribution is shown for a selected frame. RFI in this has a bandwidth of ~1.5 MHz, affects a large percentage of lines, and is very consistent in time.

bandwidth together with a comparatively small average RFI bandwidth $\mu(B_{\mathrm{RFI}})$ (not shown in Fig. 12) suggests that the center frequency of the RFI signal varies with azimuth time. This conclusion is confirmed by the RFI time-frequency plot that is shown on the right-hand side of Fig. 12(a). The overall RFI patterns in this area are consistent with the signatures of the L-band over-the-horizon radar system AN/FPS-117, manufactured by Lockheed–Martin. This system is very popular in air space surveillance and is the backbone of the North Warning System (NWS), a chain of military early warning installations. The presence of an NWS station in the analyzed area (blue symbol in Fig. 12) provides further evidence for this conclusion.

In contrast, the RFI near Odessa, Texas, shows different behavior (Fig. 13). While the number of affected lines is again high, most of the bandwidth scanned by the radar is unaffected. The interference source in this area transmits radar signals of about 1.5-Hz bandwidth at a PRF of about 1/10 of the PRF of the radar. Most importantly, in contrast to the example near Barrow, Alaska, the transmitted signal is very consistent both
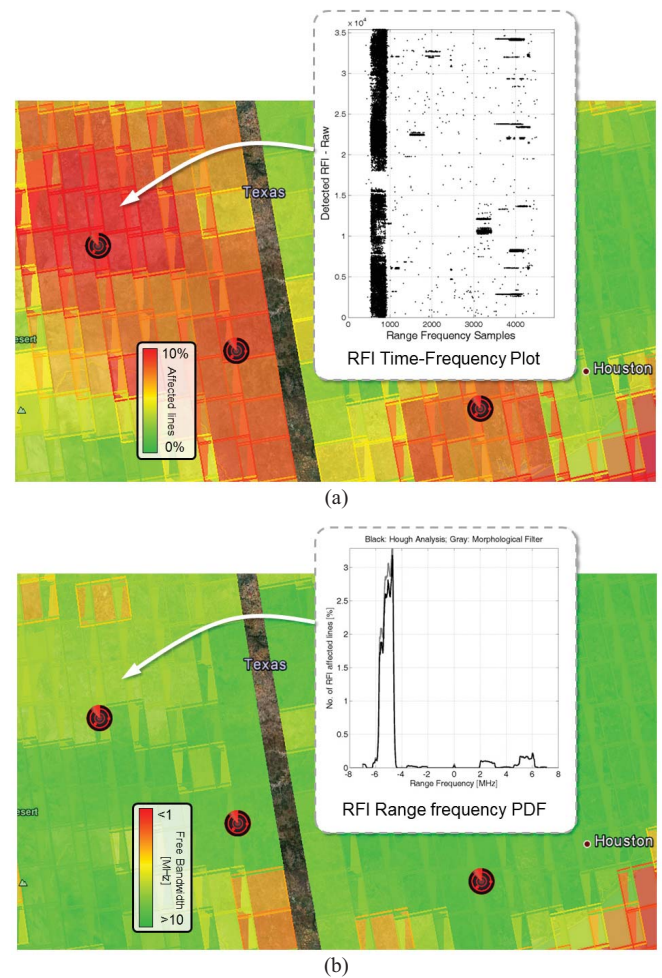
in bandwidth and center frequency. This is further emphasized by the RFI time-frequency plot shown in Fig. 13(a). Such RFI structure is consistent with the transmission patterns of the air traffic surveillance radars operated by the FAA. Locations of such stations are shown by the red circular symbols in Fig. 13, and are in good agreement with the spatial patterns of RFI in this region.

B. Multitemporal RFI Analysis

To understand the temporal stability of identified RFI patterns, repeated acquisitions over several test sites were processed and detected interference patterns were compared. Understanding the temporal stability of the statistical properties of the interfering signal is important. If it can be shown that the interference signals and their spatial distribution remain stationary over time, then the derived RFI information can be used to design future radar systems and optimize their operations. For instance, the known spatial variation of RFI time-frequency patterns could be used to perform knowledge-
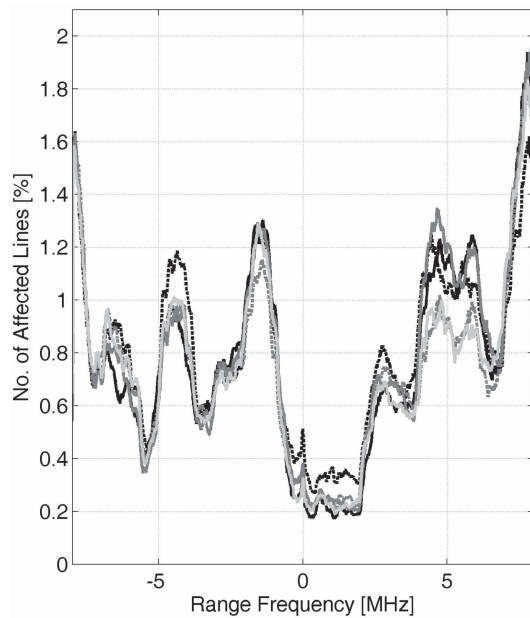
Fig. 14. RFI range-frequency PDFs for five repeat-pass ALOS PALSAR acquisitions over an area near Barrow, Alaska. Image acquisition dates include: 5/3/07 (black solid line); 3/23/09 (blue dashed line); 11/08/09 (dark-gray solid line); 11/11/10 (dark-gray dashed line); 3/29/11 (light-gray solid line).

based spatially adapted processing, where RFI filter settings are optimized to match the RFI properties in a specific area.

For all the test sites studied to date, the statistical RFI properties (RFI range frequency PDF; percentage of affected lines; ISR PDF; etc.) have remained remarkably stable. An example of this stability is shown in Fig. 14, where five multi-temporal RFI range-frequency PDFs are compared. The PDFs shown here were calculated from repeat-pass acquisitions of an image frame near Barrow, Alaska, and sample the local RFI structure for a time frame between May 3, 2007 and March 29, 2011. It can be seen that the statistical properties of the local RFI structure remained nearly unchanged over this almost four-year time span. This indicates that the processing system that was presented in this paper can produce RFI information that remains accurate and representative over long time spans. Hence, both the presented methods as well as the retrieved information can play a relevant role in the design and operations of future SAR systems operating at the analyzed frequency band.

VI. Conclusion

RF interference is a severe and growing issue in L-band radar remote sensing that affects many areas around the globe. It was shown that PALSAR data over extended areas of North America are consistently affected by complex RFI signatures, whose effects are often not sufficiently removed by traditional RFI detection and mitigation algorithms. A novel processing scheme was presented that is capable of effectively removing RFI artifacts as well as retrieving and mapping important RFI characteristics. The high performance of the RFI correction scheme was demonstrated for test areas, leading to improved image quality, polarimetric integrity, and phase noise levels.

Large-scale RFI maps were created that show that most RFI hot spots coincide with the locations of known microwave transmitters. It was further shown that an analysis of the extracted RFI data allows identification and characterization of various RFI sources. The characteristics and statistical properties of identified RFI patterns were shown to remain highly consistent over time frames of several years. This may allow the use of retrieved RFI information in system design, system operations, and adaptive data processing.

References

[1] M. Shimada, O. Isoguchi, T. Tadono, and K. Isono, "PALSAR radio-metric and geometric calibration," *IEEE Trans. Geosci. Remote Sens.*, vol. 47, no. 12, pp. 3915–3932, Dec. 2009.

[2] P. A. Rosen, S. Hensley, and C. Le, "Observations and mitigation of RFI in ALOS PALSAR SAR data: Implications for the DESDynI mission," in *Proc. IEEE Radar Conf.*, May 2008, pp. 1–6.

[3] F. J. Meyer, J. Nicoll, and A. P. Doulgeris, "Characterization and extent of randomly-changing radio frequency interference in ALOS PALSAR data," in *Proc. IEEE Int. Geosci. Remote Sens. Symp.*, Jul. 2011, pp. 2448–2451.

[4] J. E. Belz, B. L. Huneycutt, and M. W. Spencer, "A study of radio frequency interference in the space-to-Earth exploration allocation at L-band," in *Proc. IEEE Aerosp. Conf.*, Mar. 2011, pp. 1–10.

[5] A. Reigber and L. Ferro-Famil, "Interference suppression in synthesized SAR images," *IEEE Geosci. Remote Sens. Lett.*, vol. 2, no. 1, pp. 45–49, Jan. 2005.

[6] C. Le, S. Hensley, and E. Chapin, "Adaptive filtering of RFI in wideband SAR signals," in *Proc. 7th Annu. JPL Airborne Earth Sci. Workshop*, 1998, pp. 41–50.

[7] R. T. Lord and M. R. Inggs, "Efficient RFI suppression in SAR using LMS adaptive filter integrated with range/Doppler algorithm," *Electron. Lett.*, vol. 35, no. 8, pp. 629–630, Apr. 1999.

[8] F. J. Meyer, J. Nicoll, and A. P. Doulgeris, "Characterization and correction of residual RFI signatures in operationally processed ALOS PALSAR imagery," in *Proc. 9th Eur. Conf. Synth. Aperture Radar*, 2012, pp. 83–86.

[9] V. T. Vu, T. K. Sjögren, M. I. Pettersson, L. Håkansson, A. Gustavsson, and L. M. H. Ulander, "RFI suppression in ultrawideband SAR using an adaptive line enhancer," *IEEE Geosci. Remote Sens. Lett.*, vol. 7, no. 4, pp. 694–698, Oct. 2010.

[10] Z. Feng, X. Mengdao, B. Xueru, S. Guangcai, and B. Zheng, "Narrow-band interference suppression for SAR based on complex empirical mode decomposition," *IEEE Geosci. Remote Sens. Lett.*, vol. 6, no. 3, pp. 423–427, Jul. 2009.

[11] H. Zhou, B. Wen, S. Wu, and Y. Luo, "Radio frequency interference suppression in HF radars," *Electron. Lett.*, vol. 39, no. 12, pp. 925–927, Jun. 2003.

[12] P. A. Rosen, S. Hensley, and C. Chen, "Measurement and mitigation of the ionosphere in L-band interferometric SAR data," in *Proc. IEEE Radar Conf.*, May 2010, pp. 1459–1463.

[13] I. G. Cumming and F. H. Wong, *Digital Processing of Synthetic Aperture Radar Data*. Norwood, MA, USA: Artech House, 2005.

[14] R. A. Fisher, "Frequency distribution of the values of the correlation coefficient in samples from an indefinitely large population," *Biometrika*, vol. 10, no. 4, pp. 507–521, 1915.

[15] F. J. Anscombe, "Rejection of outliers," *Technometrics*, vol. 2, no. 2, pp. 123–146, 1960.

[16] D. R. Barr and E. T. Sherrill, "Mean and variance of truncated normal distributions," *Amer. Stat.*, vol. 53, no. 4, pp. 357–361, 1999.

[17] J. W. Jawitz, "Moments of truncated continuous univariate distributions," *Adv. Water Resour.*, vol. 27, no. 3, pp. 269–281, 2004.

[18] N. Aggarwal and W. C. Karl, "Line detection in images through regularized hough transform," *IEEE Trans. Image Process.*, vol. 15, no. 3, pp. 582–591, Mar. 2006.

[19] T. Risse, "Hough transform for line recognition: Complexity of evidence accumulation and cluster detection," *Comput. Vis., Graph., Image Process.*, vol. 46, no. 3, pp. 327–345, 1989.

[20] S. Buckreuss, "Filtering interferences from P-band SAR data," in *Proc. Eur. Conf. Synth. Aperture Radar*, 1998, pp. 279–282.

[21] G. Cazzaniga and A. Monti Guarnieri, "Removing RF interferences from P-band airplane SAR data," in *Proc. Int. Geosci. Remote Sens. Symp., Remote Sens. Sustainable Future*, vol. 3. May 1996, pp. 1845–1847.

[22] W. Chang, J. Li, and X. Li, "The effect of notch filter on RFI suppression," *Wireless Sensor Netw.*, vol. 1, no. 3, pp. 196–205, 2009.

[23] M. Shimada, H. Nakatani, K. Isono, and T. Kawada, "Removal of the interference appeared within the SAR images," *Adv. Space Res.*, vol. 23, no. 8, pp. 1505–1508, 1999.

[24] A. P. Doulgeris, S. N. Anfinsen, and T. Eltoft, "Automated non-Gaussian clustering of polarimetric synthetic aperture radar images," *IEEE Trans. Geosci. Remote Sens.*, vol. 49, no. 10, pp. 3665–3676, Oct. 2011.

Jeremy B. Nicoll (M'10) received the B.S. degree in chemistry and the M.S. degree in analytical chemistry from Brigham Young University, Provo, Utah, USA, in 1995 and 1997, respectively.

He has been with Fairbanks' Geophysical Institute, Alaska Satellite Facility, University of Alaska Fairbanks, Fairbanks, AK, USA, since 1998. He was a Calibration Engineer, focusing on analytical and statistical approaches to product quality. In 2001, he began developing signal processing algorithms related to SAR, with emphasis on saturation power-loss compensation. In 2003, he was appointed Lead of ASF's Technical Services Office. In 2004, he became the Engineering Center Manager. Since 2008, he was worked as the Project Engineer at the facility. His current research interests include calibration, data quality, Faraday rotation, and ionospheric effects in SAR data.

Franz J. Meyer (S'03–A'03–M'04) received the Diploma degree in geodetic engineering and the Doctor of Engineering degree from Technische Universität München, Munich, Germany, in 2000 and 2004, respectively.

He was with the Chair for Photogrammetry and Remote Sensing of the Technische Universität München, from August 2000 to September 2003, where he worked on synthetic aperture radar interferometry (InSAR) and differential InSAR. From October 2003 to February 2007, he was a Senior Remote Sensing Scientist with the Remote Sensing Technology Institute, German Aerospace Center, Oberpfaffenhofen. His scientific work was focused on InSAR techniques for current and future SAR satellites (e.g., TerraSAR-X and TerraSAR-L), the conception of algorithms for traffic monitoring using SAR satellites (e.g., TerraSAR-X), the correction and modeling of atmospheric effects in InSAR data, and persistent scatterer interferometry. From March 2007 to September 2008, he was with the Alaska Satellite Facility, University of Alaska Fairbanks, Fairbanks, AK, USA, as a Research Scientist. Since October 2008, he is with the Geophysical Institute, University of Alaska Fairbanks, where he currently holds the position of an Associate Professor for radar remote sensing. His current research interests include studies of ionospheric and tropospheric effects on SAR and InSAR, new methods of InSAR time series analysis, InSAR applications, SAR processing, and SAR data quality analysis. He is the author of more than 80 scientific publications, including four being acknowledged as "Best Papers."

Dr. Meyer was the recipient of the IEEE Geoscience and Remote Sensing Society Gold Early Career Award 2011 for demonstrating outstanding ability and promise for significant contributions in the future.

Anthony P. Doulgeris (S'06–M'12) received the B.Sc. degree in physics from the Australian National University, Canberra, Australia, in 1988, the M.Sc. degree and the Ph.D. degree in physics from the Department of Physics and Technology, University of Tromsø, Tromsø, Norway, in 2006 and 2011, respectively.

He is continuing his research in applied Earth observation as a Post-Doctoral Research Fellow with the Department of Physics and Technology, University of Tromsø, Tromsø, Norway, and is with the Barents Remote Sensing School. His current research interests include investigating remote sensing, pattern recognition, and multidimensional statistical modeling, in particular with polarimetric synthetic aperture radar images.